# Supplementary Information

Stefan Wild, [a] Bruno Lacerda de Oliveira Campos, [a] Thomas A. Zevaco, [a] David Guse, [b] Matthias Kind, [b] Stephan Pitter, [a] Karla Herrera Delgado, [*a] and Jörg Sauer [a]

[a] IKFT - Institute of Catalysis Research and Technology, Karlsruhe Institute of Technology, Hermann-von-Helmholtz-Platz 1, D-76344 Eggenstein-Leopoldshafen, Germany. E-mail: karla.herrera@kit.edu

[b] TVT - Institute of Thermal Process Engineering, Karlsruhe Institute of Technology, Kaiserstraße 12, D-76131 Karlsruhe, Germany.

## Table of Content

# 1 Carbon balance calculation

The carbon balance was calculated according to (eq S1).

$$C - balance = \frac{\dot{n}_{CO,in} + \dot{n}_{CO_2,in} - (\dot{n}_{MeOH,out} + 2 * \dot{n}_{DME,out} + \dot{n}_{CO,out} + \dot{n}_{CO_2,out} + \sum \nu_x \dot{n}_{C_xH_y})}{\dot{n}_{CO,in} + \dot{n}_{CO_2,in}} \quad \text{(eq S1)}$$

# 2 Loop variation

The measuring procedure with varying inlet-feed concentration, temperature, catalyst bed and recurring purging is shown in Fig S1.

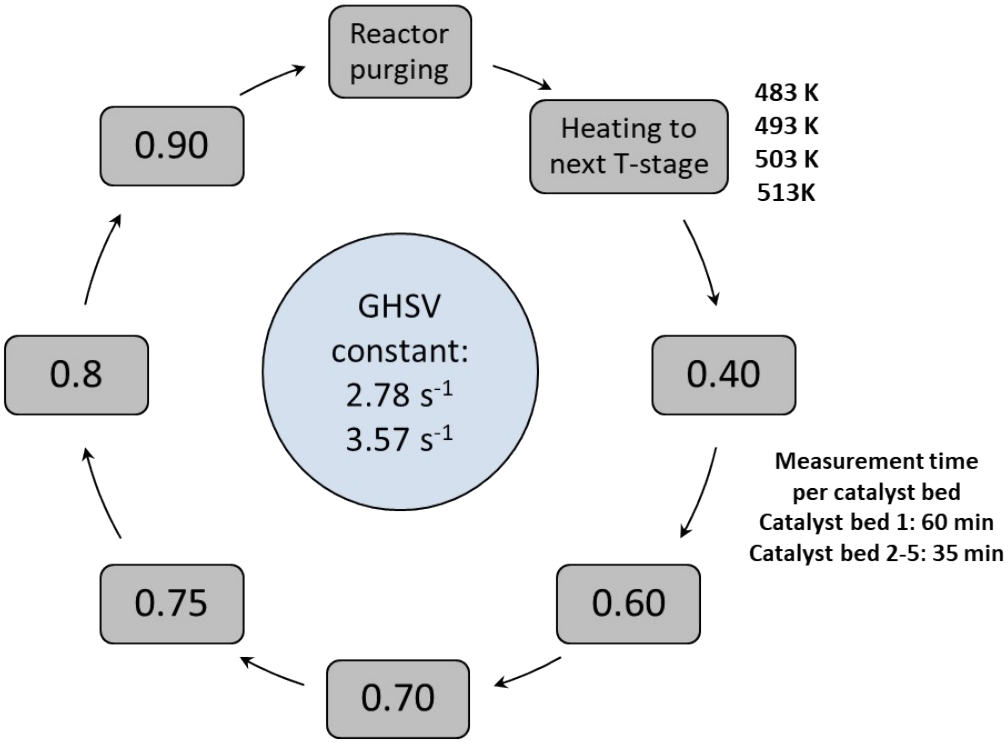


**Fig S1: Schematic illustration of the procedure of varying reaction conditions at a constant GHSV with recurring reference point at 50 bar.**

Each GHSV was measured by varying the feed concentration within one reactor temperature. The pressure was constantly at 30 bar for all experiments.

# 3 Calculation of possible errors in single and parallel operation mode

The error estimation of the MURSS2 plant (Manuscript: Figure 1 and Fig S2) took place with the operation of all six reactors. The aim of the error estimation was to prove experimentally whether the same product (MeOH) concentrations could be achieved under the same intended operating conditions in each reactor. Therefore, an industrially MeOH catalyst ($Cu/ZnO/Al_2O_3$) was filled in each of the six reactors with equal amounts of

mass (3.0 g), SiC dilution (15.0 g), and catalyst bed length (ca. 55 mm). The operating conditions were: 493 K, 30 bar, a catalyst mass specific GHSV of 14 $l_N/(g_{cat} \cdot h)$ and a syngas feed of $CO/CO_2/H_2/N_2$ = 12/3/38/48 vol.%. In order to eliminate the error of a non-uniform distribution of an additional catalyst component, no dehydration component was added. The MeOH output concentration is taken as reference for the analysis, measured via FTIR. The reactors were operated in single and parallel operation mode to compare the MeOH production in the respective operation modes. The relevant error sources from measured variables such as x, y, z etc. are included in the calculation of the total error $u_f$ of the error function f(x,y,z) according to (eq S2).

$$u_f = \sqrt{\left(\frac{\delta f}{\delta x}\sigma_x\right)^2 + \left(\frac{\delta f}{\delta y}\sigma_y\right)^2 + \left(\frac{\delta f}{\delta z}\sigma_z\right)^2 + \dots} \qquad \text{(eq S2)}$$

**Fig S2: MURSS (Multi-reactor-screening-system) with opened reactor-insulations.**

Subsequently, possible sources of error are estimated and, if necessary, quantified with regard to the measured MeOH concentration. Beside MeOH no oxygenates or hydrocarbon-products with concentrations above 0.01 vol.% could be detected.

## 3.1 Errors in bed temperature

Deviating bed temperatures (without reaction) are measured in each individual reactor with the same thermocouple (TC) in order to exclude limit deviations of six different TC (NiCr-Ni type K). Despite the temperature correction, deviations from the setpoint temperature can be detected in the catalyst bed (Fig S3).

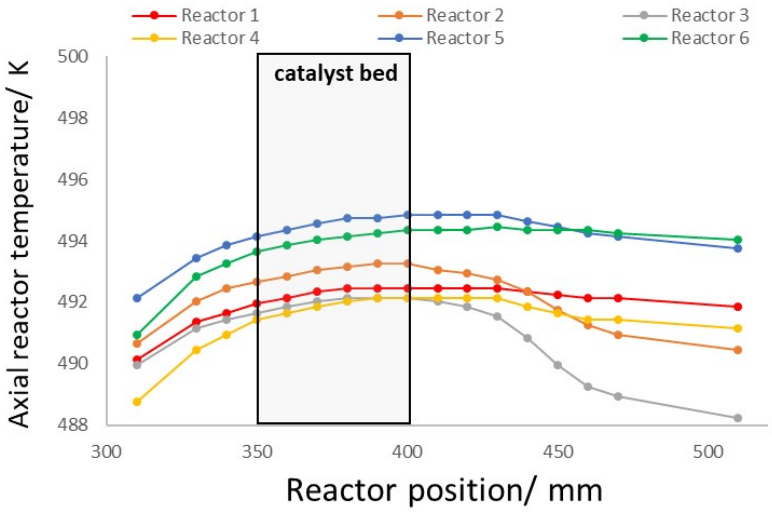


**Fig S3: Axial reactor temperature of reactor 1-6 for setpoint temperature 493 K at 30 bar $N_2$-volume flow: 0.7 $l_N$/(min·reactor).**

For the respective reactor temperatures 1-6 in the catalyst bed, between 350 and 400 mm, the mean value of six axial temperature measurement points is calculated. The resulting average bed temperatures are shown Table S1.

**Table S1: Mean catalyst bed temperatures (350-400 mm) of reactor 1-6 for temperature setpoint 493 K at 30 bar and 0.7 $l_N$/(min·reactor) $N_2$ volume flow.**

| Reactor i | $T_{0,i}$ :Mean catalyst bed temperature / K |
|---|---|
| 1 | 492.4 |
| 2 | 493.1 |
| 3 | 492.1 |
| 4 | 492.0 |
| 5 | 494.7 |
| 6 | 494.2 |
| **Mean value/ K** | 493.1 |

The sample standard deviation $\sigma_{T0}$ from these n = 6 mean catalyst bed temperatures $T_{0,i}$ is calculated via (eq. S3).

$$\sigma_{T0} = \sqrt{\frac{1}{n-1}\sum_{i=1}^{n}(T_{0,i} - \bar{T}_0)^2} = \pm 1.12\ K \qquad \text{(eq. S3)}$$

Where $\bar{T}_0$ is the arithmetic mean temperature of the $n$ = 6 measured axial catalyst bed temperatures (see Fig S3). Using the finite difference method, the sensitivity of the MeOH concentration to the mean catalyst bed temperature ($\delta y_{MeOH} / \delta T_0$) can be determined experimentally or by a suitable MeOH-kinetic

model. Using the microkinetic model of Campos et al.[1] determines $\delta y_{MeOH} / \delta T_0$ with a temperature bed variation of ±h/2 K:

$$\frac{\delta y_{MeOH}}{\delta T_0} = \frac{y_{MeOH\_model}\left(T = 493\ K + \frac{h}{2}\right) - y_{MeOH\_model}\left(T = 493\ K - \frac{h}{2}\right)}{h} \quad \text{(eq S4)}$$

For h = 2 K the model-based value for the sensitivity of MeOH-concentration to the mean catalyst bed temperature is determined to:

$$\frac{\delta y_{MeOH}}{\delta T_0} = 0{,}0288\ vol.\%_{MeOH}/K$$

As a result, the error $u_{y_{-MeOH_{T0}}}$ by the deviating catalyst bed temperatures is calculated via (eq.S5).

$$u_{y_{-MeOH_{T0}}} = \frac{\delta y_{MeOH}}{\delta T_0} * \frac{\sigma_{T0}}{\bar{y}_{MeOH-single}} = \pm 1.60\ \% \quad \text{(eq.S5)}$$

## 3.2 Errors in reactor pressure

Since the MeOH synthesis from CO resp. $CO_2$ hydrogenation is pressure dependent (see manuscript: R1 resp. R2), potential pressure differences between reactors must be considered. A common pressure valve (PIRC) at the end of the exhaust line (Figure 1) controls the pressure in all reactors, so that pressure differences between the reactors can only result from unequal pressure losses in the respective reactor trains 1-6 (see Figure 1). Since the same valves and fittings are used in each reactor train, pressure differences can only occur due to the different lengths of 1/8" piping up to the pressure valve. For compressible media, the pressure drop across a pipe is calculated using (eq S6)[2].

$$\Delta p = p \cdot \left(1 - \sqrt{1 - \frac{\lambda \cdot l \cdot \rho \cdot c^2}{d \cdot p}}\right) \quad \text{(eq S6)}$$

λ: pipe friction coefficient

l: Length of the flowed pipe

ρ: Density of the fluid

c : Fluid speed

d: Internal diameter of the flowed pipe

p: Pressure at the beginning of the pipe

For the estimation of the different pressure losses, nitrogen is considered as a fluid under a maximum standard flow rate per reactor of 2 $l_N$/(min·reactor), pipe temperature 298 K and a set pressure of 30 bar at PIRC (Manuscript: Figure1). Higher volume flows resp. flow speeds are not expected in the current plant set-up. For the maximum pressure difference between two reactors, the longest 1/8” pipeline (reactor 1: 2.9 m) was compared with the shortest one (reactor 6: 1.5 m).

To calculate the pressure loss, the pipe friction coefficient λ must be known. In order to calculate this value, it is necessary to know the Reynolds number (Re) of the flow. This is calculated as follows:

$$Re = \frac{c \cdot d}{\nu} \qquad \text{(eq S7)}$$

The coefficient of pipe friction is determined according to the type of flow either laminar (eq S8) (laminar):

$$\lambda = \frac{64}{Re} \qquad \text{(eq S8)}$$

or in the case of a turbulent flow via the law of Blasius (eq S9):

$$\lambda = \frac{0{,}3614}{Re^{0{,}25}} \qquad \text{(eq S9)}$$

The dynamic viscosity $\eta_{T,P}$ at a given temperature T at a pressure p can be approximated using (eq S10[3]:

$$\eta_{T,p} = \eta_0 \cdot e^{\cdot p/T} \qquad \text{(eq S10)}$$

For the reactor strands considered (1 and 6), (eq S6) gives the following pressure losses:

$\Delta p$ reactor1: = 278 Pa

$\Delta p$ reactor6: = 144 Pa

The maximum pressure difference between two reactors in the parallel reactor plant is therefore 134 Pa. A maximum, relative deviation in reactor pressure of 0.0045% is achieved for the operating conditions considered (3 MPa). The influence of different reactor pressures is therefore neglected.

## 3.3 Error due to differing catalyst masses

The used precision balance of *ströhlein* has a measuring accuracy of ±100 µg. At a minimum catalyst mass of 0.0526 g (H-FER 20), this results in a maximum relative error of ±0.19%. Errors caused by differing catalyst balances are therefore neglected.

## 3.4 Error caused by analytics

For the error estimation, an FTIR CX4000 (Gasmet Technologies Oy) was used which measures with an analytical accuracy of relative ±1.00% for instrument calibrated species (MeOH was calibrated by the manufacturer). This source of error is therefore taken into account in the error estimation.

## 3.5 Error caused by hot spot formation

The MeOH-forming component CZA was filled in the reactor with a SiC/CZA dilution of 5:1. Therefore, an non-uniform distribution of the active species in the inert material can lead to the formation of hot spots in axial and radial direction and thus to differences in the activity of each catalyst bed. In the CZZ/FER variation experiments, the MeOH-catalyst mass-specific SiC/CZZ dilution was at least 10:1 and was made up with a fivefold partition to ensure improved distribution of the active material and to reduce the error due to hot spot formation.

As the error due to catalyst bed hot spots $u_{y\_MeOH,Hot-Spots}$ is hard to determine experimentally with the existing set-up, this error was calculated indirectly (eq S11) by the experimental determined MeOH concentration error in single reactor operation $u_{y\_MeOH,single}$ with a deviation of ±2.65%, the experimentally available relative error $u_{y_{-MeOH}T0}$(±1.60%) calculated in S3.1 and the manufacturer information of the used FTIR: $u_{MeOH,FTIR}$ (±1.00 %).

$$u_{y\_MeOH\_single} = \sqrt{\left(\frac{\delta y_{MeOH}}{\delta T_0}\sigma_{T0}\right)^2 + \left(u_{MeOH,Hot-Spots}\right)^2 + \left(u_{y_{-MeOH\_FTIR}}\right)^2} \qquad \text{(eq S11)}$$

The resulting relative error $u_{MeOH,Hot-Spots}$ is ±1.86%. This error includes all unknown and neglected errors and is probably higher than it would be if the error was measurable.

## 3.6 Error caused by parallel operation

The error propagation function $u_{y\_MeOH\_Parallel}$ in the case of parallel operation mode is:

$$u_{y\_MeOH\_Parallel} = \sqrt{\left(\frac{\delta y_{MeOH}}{\delta T_0}\sigma_{T0}\right)^2 + \left(u_{MeOH,Hot-Spots}\right)^2 + \left(u_{y_{-MeOH\_FTIR}}\right)^2 + \left(\frac{\delta y_{MeOH}}{\delta GHSV}\sigma_{GHSV}\right)^2} \qquad \text{(eq S12)}$$

Fig S4 shows the fluctuating reactor GHSV within an experimental duration of 190 min. To calculate $u_{y\_MeOH\_parallel}$ the information of the flow meters in front of each reactor (Fig1) can be used. Measuring the standard deviation of the reactor volume flow causing the standard deviation of GHSV ((eq S13)) and as a result the error in MeOH concentration. This calculation method is also introduced to prove the accuracy of the flow meters and the determined fluctuations of the GHSV during the experiments (Fig S4).

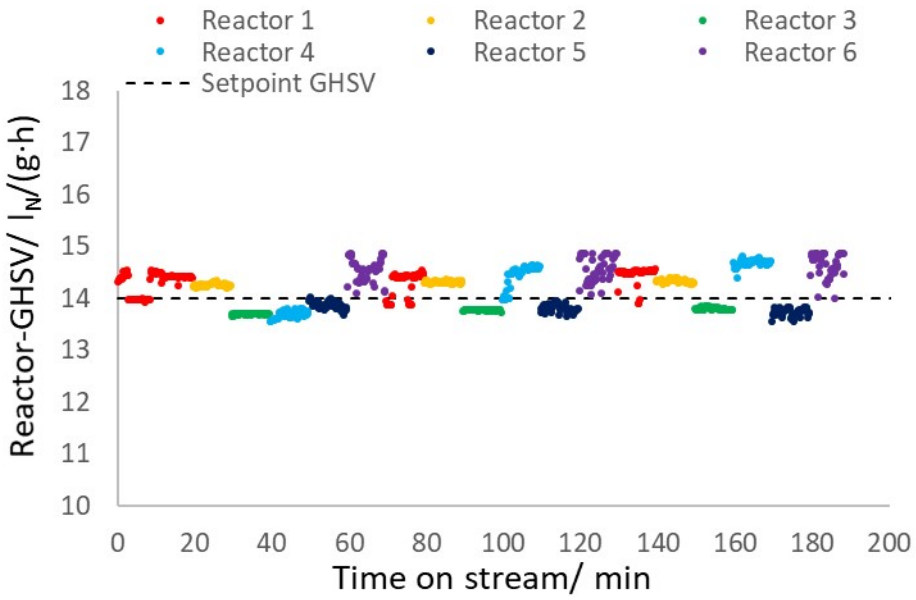


**Fig S4: Fluctuation of reactor GHSV for each reactor, measured in ToS of approx. 190 min.**

The respective standard deviation of the GHSV is calculated via (eq S13).

$$\sigma_{GHSV} = \sqrt{\frac{1}{n-1}\sum_{i=1}^{n}\left(GHSV_i - \bar{GHSV}\right)^2} = \pm 0.51\ l_N/(g*h) \qquad \text{(eq S13)}$$

The MeOH sensitivity of GHSV deviation $\delta y_{MeOH}/\delta GHSV$ was determined experimentally (Fig S5) for a GHSV range typically expected within the operation of the parallel reactor plant. Experimental conditions were: 493 K, 30 bar and a catalyst mass specific GHSV of 14 $l_N/(g_{cat}\cdot h)$ and feed of 12/3/38/48 vol.% $CO/CO_2/H_2/N_2$. For the GHSV range of 12 to 36 $l_N/(g\cdot h)$ considered in the parallel reactor plant, the second degree polynomial compensation function shows a coefficient of determination $R^2$ of 0.9981, showing a good approximation of the sensitivity of MeOH concentration as a function of GHSV.

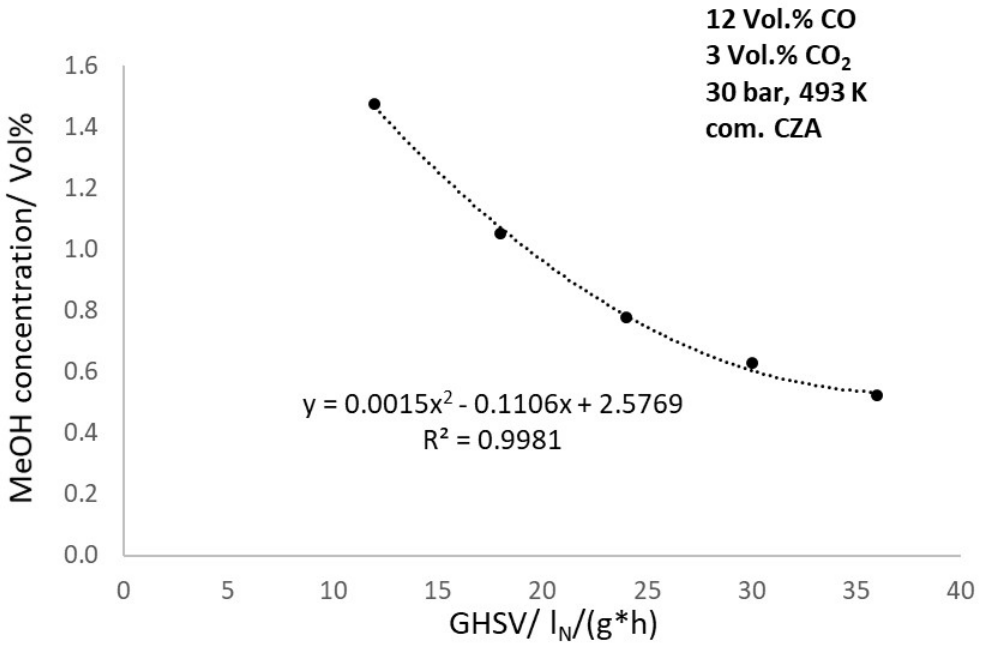


**Fig S5: Experimental determination of the MeOH sensitivity by variation of the GHSV.**

The MeOH sensitivity of GHSV deviation $\delta y_{MeOH} / \delta GHSV$ was calculated for a GHSV range typically expected within the operation of the parallel reactor plant calculating the derivation of the compensation function *y* (see Fig S5) at a GHSV value of 14 $l_N/(g \cdot h)$ resulting in a value of -0.0686 vol.% MeOH/$l_N/(g \cdot h)$. As a result, the error $u_{y\text{-}MeOH_{GHSV}}$ can be calculated via (eq S14):

$$u_{y\text{-}MeOH_{GHSV}} = \frac{\delta y_{MeOH}}{\delta GHSV} * \frac{\sigma_{GHSV}}{\bar{y}_{MeOH-parallel}} = \pm 1.48\,\% \qquad \text{(eq S14)}$$

## 3.7 Alternative GHSV error calculation

With (eq S12) the additional error $u_{y\text{-}MeOH_{GHSV}}$ can be calculated in the same indirect way as $u_{MeOH,Hot-Spots}$ using the previously calculated error $u_{MeOH,Hot-Spots}$ and the experimentally known relative error of MeOH concentration in parallel operation $u_{y\_MeOH\_parallel}$ (±2.89 %). This calculation method leads to a relative error for $u_{y\text{-}MeOH_{GHSV}}$ of ±1.16 %. Both error values for GHSV deviation (±1.48%, see S3.6 and ±1.16 %) indicate an acceptable additional error in parallel operation mode and confirm that the parallel reactor system is capable of providing high-quality kinetic data.

# 4 Additional results within parameter variation

Graphs for DME and MeOH productivities, which complement the graphs in the manuscript (Figure 3) are shown in Fig S6 for $CO_2/CO_x$ inlet ratios of 0.4 (a), 0.7 (b) and 0.8 (c), four different temperatures between 483 and 513 K under variation of $\zeta_{CZZ}$ at 2.78 $s^{-1}$ and 30 bar. The dashed lines show the simulated values and the dots the experimentally measured values for MeOH (framed dots) and DME (unframed dots), respectively.

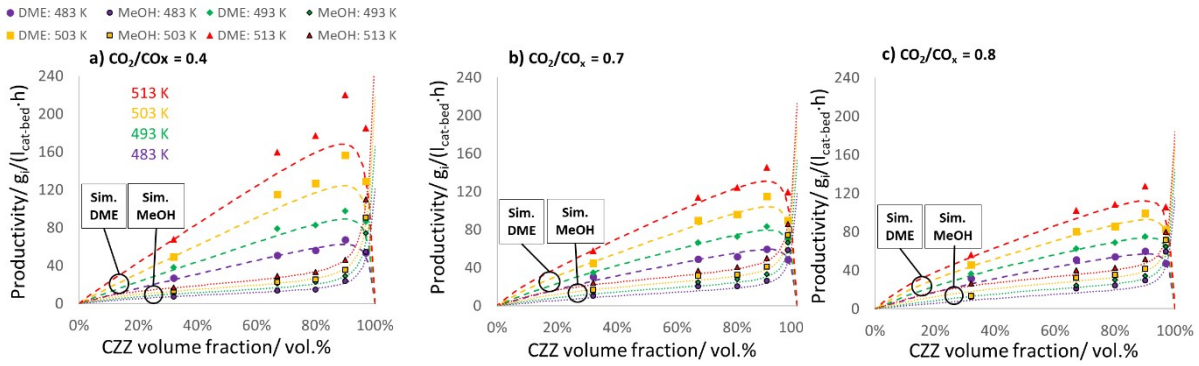


**Fig S6: DME and MeOH productivities for $CO_2/CO_x$ inlet ratios of 0.4 (a), 0.7 (b) and 0.8 (c) with 20 vol.% total $CO_x$ in feed at 483-513 K, 2.78 $s^{-1}$ and 30 bar.**

Graphs for $CO_2$ and CO conversions, which complement the graphs in the manuscript (Figure 4), are shown in Fig S7 for $CO_2/CO_x$ of 0.4 (a), 0.7 (b), 0.8 (c) at 2.78 $s^{-1}$ and 30 bar. The dashed lines show the simulated values and the dots the experimentally measured values for the conversion of $CO_2$ (framed dots) and CO (unframed dots), respectively.

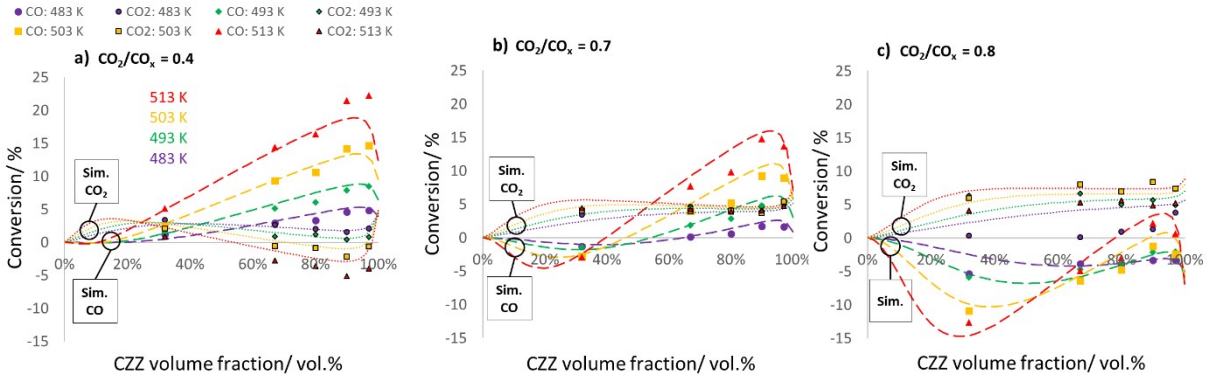


**Fig S7: $CO_2$ and CO conversion for $CO_2/CO_x$ inlet ratios of 0.4 (a), 0.7 (b) and 0.8 (c) with 20 vol.% total $CO_x$ in feed at 483-513 K, 2.78 $s^{-1}$ and 30 bar.**

Graphs for MeOH and DME selectivity, which complement the graphs in the manuscript (Figure 5), are shown in Fig S8 for $CO_2/CO_x$ of 0.4 (a), 0.7 (b), 0.8 (c) at 2.78 $s^{-1}$ and 30 bar. The dashed lines show the simulated values and the dots the experimentally measured values for MeOH (framed dots) and DME (unframed dots), respectively.

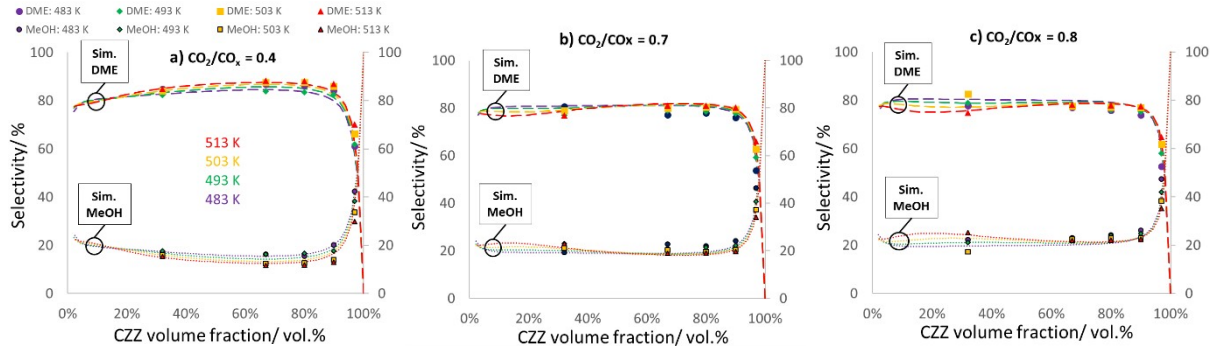


**Fig S8: MeOH and DME selectivity for $CO_2/CO_x$ inlet ratios of 0.4 (a), 0.7 (b) and 0.8 (c) with 20 vol.% total $CO_x$ in feed at 483-513 K, 2.78 $s^{-1}$ and 30 bar.**

# 5 Water evaluation under parameter variation

Fig S9 shows the simulated water selectivity calculated via eq S15.

$$S_{H_2O,H_2} = \frac{\dot{n}_{H_2O,out}}{\dot{n}_{H_2,in} - \dot{n}_{H_2,out}} \qquad \text{(eq S15)}$$

The water selectivity in Fig S9 is shown for different $CO_2/CO_x$ inlet ratios of 0.4 (a), 0.6 (b), 0.7 (c), 0.75 (d), 0.8 (e) and 0.9 (f) at four different temperatures between 483 and 513 K under variation of $\zeta_{CZZ}$ and a GHSV of 2.78 $s^{-1}$.

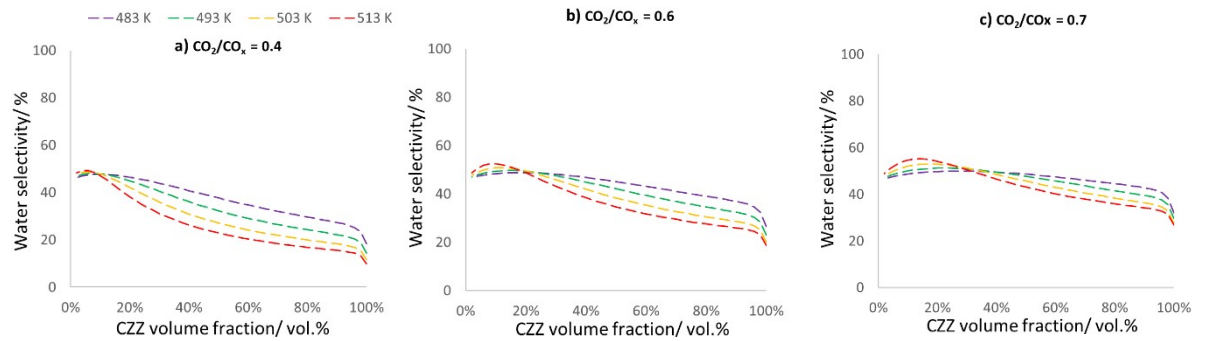

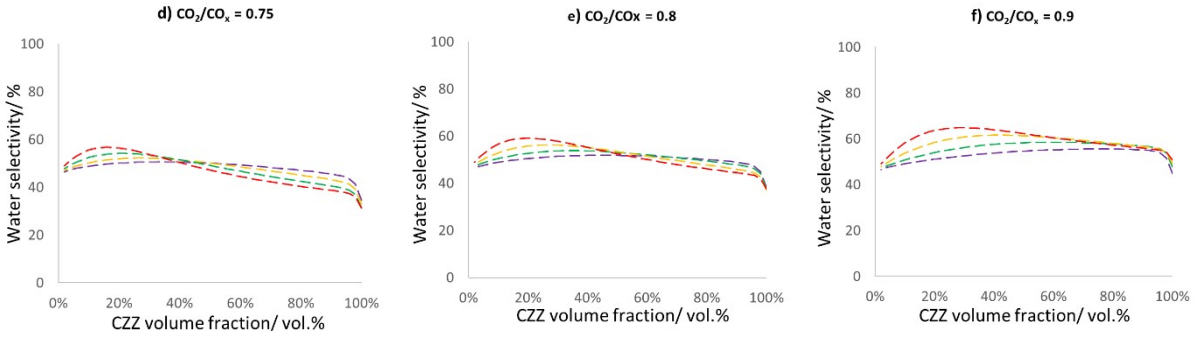


**Fig S9: Simulated water selectivity at 483-513 K, 30 bar, 2.78 $s^{-1}$, for $CO_2/CO_x$ inlet ratios of 0.4 (a), 0.6 (b), 0.7 (c), 0.75 (d), 0.8 (e), and 0.9 (f) with 20 vol.% total $CO_x$ in feed.**

Comparing the patterns of water selectivity with DME selectivity as shown in the manuscript (Figure 5) and in the SI (Fig S8), an influence of water selectivity on DME selectivity is evident. As the water selectivity increases, the DME selectivity is negatively affected, resulting in more non-dehydrated MeOH.

# 6 Thermodynamic equilibrium at kinetic measurement conditions

Fig S10 shows the simulated $CO_x$ conversions for $CO_2/CO_x$ inlet ratios of 0.4 (a), 0.6 (b), 0.7 (c), 0.75 (d), 0.8 (e) and 0.9 (f) at four different temperatures between 483 and 513 K under variation of $\zeta_{CZZ}$ and a GHSV of 2.78 $s^{-1}$.

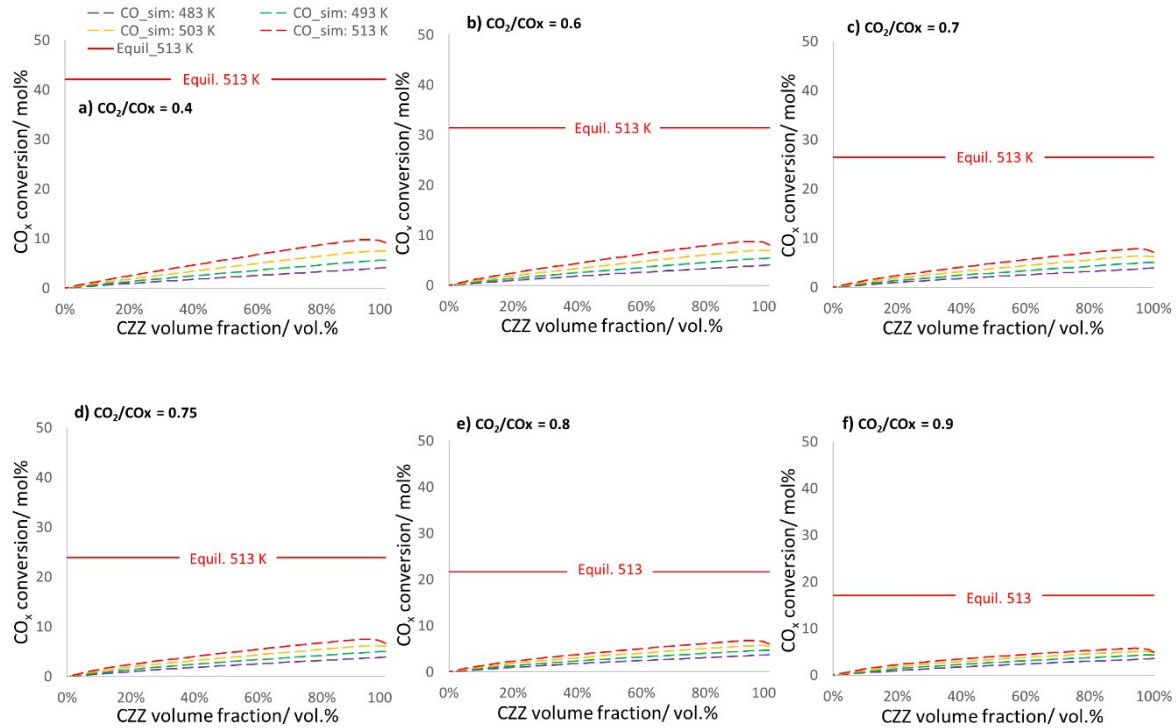


**Fig S10: Simulated $CO_x$ conversion at 483-513 K, 2.78 $s^{-1}$ and 30 bar and the respective thermodynamic equilibrium for $CO_2/CO_x$ inlet ratios of 0.4 (a), 0.6 (b), 0.7 (c), 0.75 (d), 0.8 (e), and 0.9 (f) with 20 vol.% total $CO_x$ in feed.**

It can be seen that for each $CO_2/CO_x$ inlet ratio investigated, the thermodynamic equilibrium is far enough away from the simulated curves, proving a kinetically controlled regime for all measured data points.

# 7 High performance conditions

In Fig S11 an industrial interesting operating range with “high performance” (H.P.) conditions is shown. With a syngas ($CO_2/CO_x$ = 0.6) without $N_2$-dilution, at increased pressure (60 bar) and a higher $H_2$ feed concentration (70 vol.%) compared to kinetic measurement conditions ($H_2/CO_x/N_2$ = 45/20/35 vol.%) using an optimized CZZ/FER bed ratio allows $CO_x$ conversion above 47 mol.% for GHSV below 0.4 $s^{-1}$.

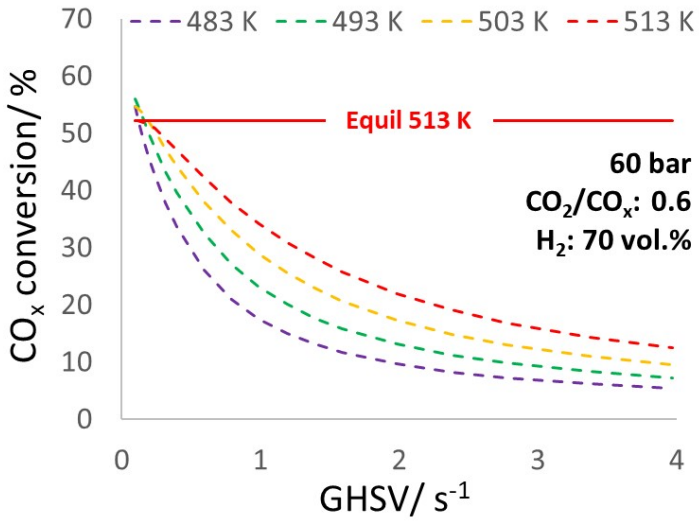


**Fig S11: Simulated $CO_x$ conversion at 483-513 K, 0.397 $s^{-1}$ and 60 bar and the respective thermodynamic equilibrium at 513 K for $CO_2/CO_x$ inlet ratio of 0.6 with 30 vol.% total $CO_x$ in feed.**

The respective contour plot for an optimal FER volume fraction in view of DME productivity as function of temperature and GHSV at H.P. conditions is shown in Fig S12.

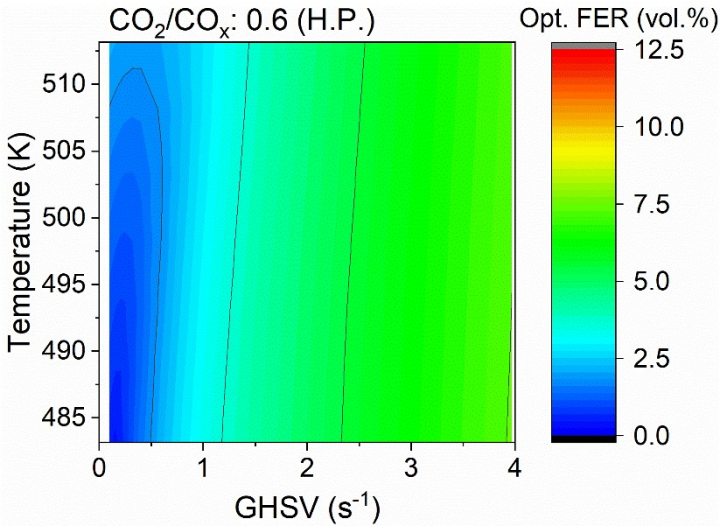


**Fig S12: Contour plot of optimal FER volume fraction in view of DME productivity under variation of temperature and GHSV at H.P. conditions: 60 bar, 70 vol.% $H_2$ and a $CO_2/CO_x$ inlet ratio of 0.6 with 30 vol.% total $CO_x$ in feed.**

The low temperature dependence of the optimal FER content at elevated GHSV is again clearly visible. However, compared to the plots shown in the manuscript, the temperature dependence is less pronounced at lower GHSV. The H.P. conditions show that at near-equilibrium $CO_x$ conversions (Fig S11), FER volume fractions below 3% are enough to achieve optimal DME productivity.

# 8 Axial temperature profiles under reaction conditions

To ensure isotherm reaction conditions for the data required for the modelling axial temperature profiles were measured. The highest heat formation within the parameter variation (Table 3) was expected at 513 K, $CO_2/CO_x$ ratio of 0.4, at 2.78 $s^{-1}$ and 30 bar with a CZZ/FER ratio of 90/10 (Fig S6a). The axial bed-temperature increase

due to the exothermic reactions R1 - R4 was determined by the temperature difference (Fig S13c) between a reference measurement under $N_2$-Flow (Fig S13a) and the respective axial bed temperature under the reaction conditions (Fig S13b) mentioned above. The axial temperature profile shows a maximum of $\Delta T = 1.1$ K. This verifies the assumption of isothermal operating conditions within the parameter variation considered.

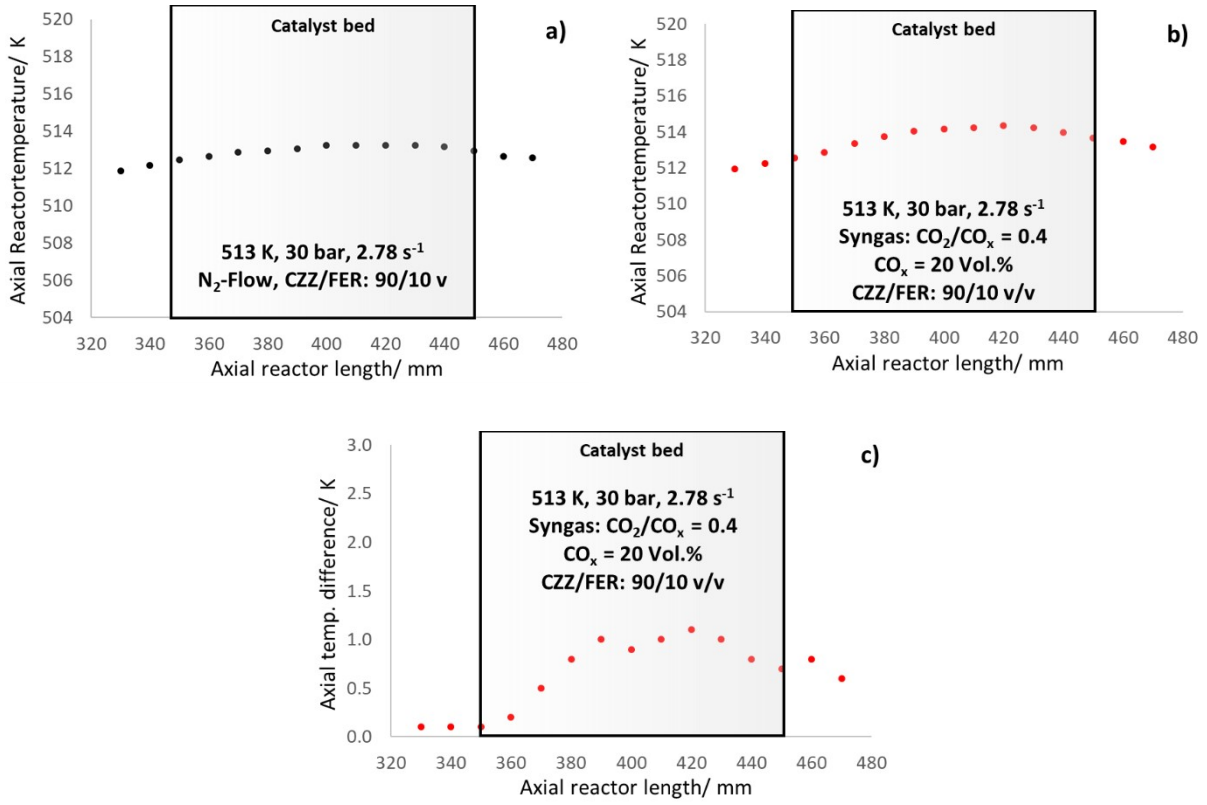


**Fig S13: Axial reactor temperature profiles under $N_2$-flow (a), syngas: $CO_2/CO_x = 0.4$, with 20 vol.% total $CO_x$ in feed and the respective axial temperature difference (c) along the catalyst bed (350-450 mm), at 30 bar and 2.78 $s^{-1}$.**

# 9 XRD analysis of the CZZ pre-catalyst

The XRD analysis was performed under the conditions and methodology described from Polierer et al.[4] to get information of the phase composition, CuO particle size and the crystalline/amorphous characteristics of the CZZ catalyst in the calcined and precursor stage. In Fig S14 the XRD pattern of the CZZ precursor material is shown with the references of malachite (Intensities (I) from Swanson et al.[5], $I \geq 20\%$) and rosasite (Roberts et al.[6], $I \geq 30\%$).

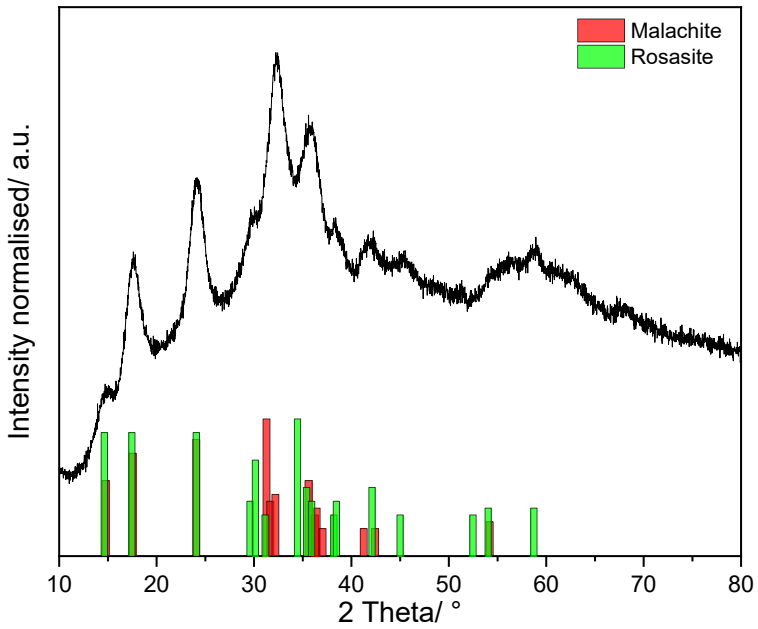


**Fig S14: XRD pattern of the CZZ precursor with references of malachite and rosasite[6].**

The most intensive reflection for the non-calcined CZZ precursor at 32.2° results from the overlapping main reflections of malachite (31.3, 31.7 and 32.2°). The slightly distinct shoulder at 30.0° indicates shares of rosasite. The reflexes at 17.5° and 24.3° results from the overlapping high intensities of rosasite (17.47° and 24.1°) and malachite (17.53° and 24.1°). To investigate the composition of the as-obtained malachite-containing catalyst precursor, *rietveld* refinement was performed with the program *profex*[7]. Under the consideration of the lattice parameters, the Zn content in the malachite phase can be estimated as reported from Behrens et al.[8]. The malachite fraction is 97.7% with a Zn content of 24% ±6%. Moreover, the *rietveld* analysis of the diffraction pattern of the calcined pre-catalyst has been conducted to investigate crystallite sizes resulted in CuO particle sizes of 7 nm ± 1 nm. In Fig 15 the XRD pattern of the calcined pre-catalyst is shown with references of monoclinic CuO (from Brese et al.[9], I > 15%) and ZnO (from Sawada et al.[10], I > 20%).

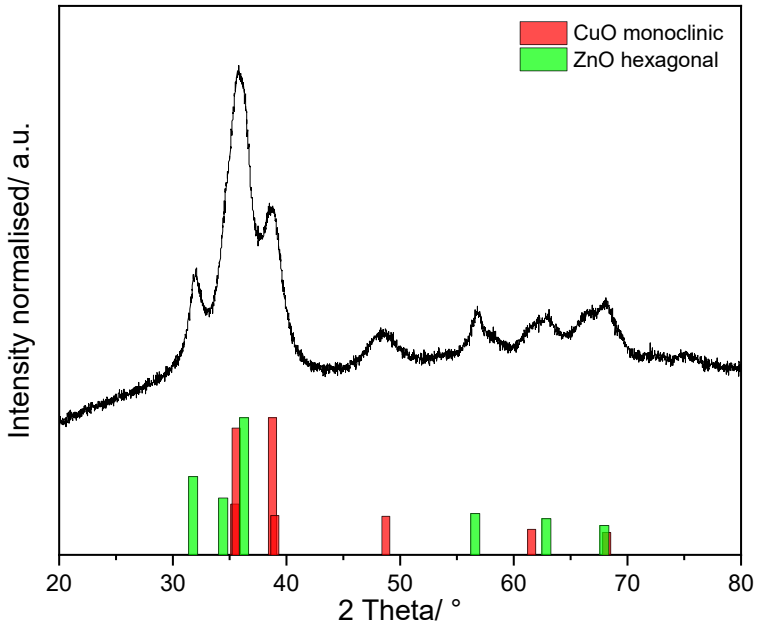


**Fig 15: XRD pattern of the calcined CZZ catalyst with references of monoclinic CuO[9] and hexagonal ZnO[10].**

For the calcined pre-catalyst the most intensive reflection at 35.6° results from the overlapping main reflection of CuO (35.6°) and ZnO (34.4° and 36.2°). Pronounced reflections are seen for CuO at 38.8° and 48.7° and for ZnO at 31.8° and 56.6°. The reflexes show a slight widening, which is probably due to the small particle size (see manuscript, Table 4).

# 10 Derivation: Reaction rate MeOH dehydration

The associative path of the methanol dehydration consists in two reactions:

$$R_1\text{: } CH_3OH_{(g)} + (d) \rightleftarrows CH_3OH_{(d)} \quad \text{(eq S16)}$$

$$R_2\text{: } CH_3OH_{(g)} + CH_3OH_{(d)} \rightleftarrows CH_3OCH_{3(g)} + H_2O_{(g)} + (d) \quad \text{(eq S17)}$$

Where (d) is a free FER active site. DME and water formation ($R_2$) is the rate determining step (RDS) of this reaction path[11]. Therefore, we assume that methanol adsorption ($R_1$) is in quasi-equilibrium, that is:

$$k_1^+ \gg r_1 \qquad or \qquad \frac{r_1}{k_1^+} \approx 0 \quad \text{(eq S18)}$$

Where $k_1^+$ is the kinetic constant of forward elementary reaction 1, and $r_1$ is the reaction rate of reversible elementary reaction 1. The elementary equilibrium constant ($K_1$) is defined as:

$$K_1 = \frac{k_1^+}{k_1^-} \quad \text{(eq S19)}$$

By substituting eqs. (S18-S19) into the reaction rate equation (eq S20), it is then possible to calculate the coverage of methanol on the catalyst surface:

$$r_1 = m_{FER} \cdot (k_1^+ \cdot f_{CH_3OH} \cdot \theta_d - k_1^- \cdot \theta_{CH_3OH_{(d)}}) \quad \text{(eq S20)}$$

$$r_1 = m_{FER} \cdot k_1^+ \cdot \left( f_{CH_3OH} \cdot \theta_d - \frac{k_1^-}{k_1^+} \cdot \theta_{CH_3OH_{(d)}} \right) \quad \text{(eq S21)}$$

$$r_1 = m_{FER} \cdot k_1^+ \cdot \left( f_{CH_3OH} \cdot \theta_d - \frac{\theta_{CH_3OH_{(d)}}}{K_1} \right) \quad \text{(eq S22)}$$

$$\frac{r_1}{k_1^+} = m_{FER} \cdot \left( f_{CH_3OH} \cdot \theta_d - \frac{\theta_{CH_3OH_{(d)}}}{K_1} \right) \quad \text{(eq S23)}$$

$$0 = m_{FER} \cdot \left( f_{CH_3OH} \cdot \theta_d - \frac{\theta_{CH_3OH_{(d)}}}{K_1} \right) \quad \text{(eq S24)}$$

$$\theta_{CH_3OH_{(d)}} = f_{CH_3OH} \cdot \theta_d \cdot K_1 \quad \text{(eq S25)}$$

The reaction rate equation of elementary reaction 2 (eq S17) is defined as:

$$r_2 = m_{FER} \cdot (k_2^+ \cdot \theta_{CH_3OH_{(d)}} \cdot f_{CH_3OH} - k_2^- \cdot f_{DME} \cdot f_{H_2O} \cdot \theta_d) \quad \text{(eq S26)}$$

$$r_2 = m_{FER} \cdot k_2^+ \cdot \left( \theta_{CH_3OH_{(d)}} \cdot f_{CH_3OH} - \frac{k_2^-}{k_2^+} \cdot f_{DME} \cdot f_{H_2O} \cdot \theta_d \right) \quad \text{(eq S27)}$$

Substituting eq S25 and introducing the elementary equilibrium constant of reaction 2 ($K_2$):

$$r_2 = m_{FER} \cdot k_2^+ \cdot \left( f_{CH_3OH} \cdot \theta_d \cdot K_1 \cdot f_{CH_3OH} - \frac{1}{K_2} \cdot f_{DME} \cdot f_{H_2O} \cdot \theta_d \right) \quad \text{(eq S28)}$$

$$r_2 = m_{FER} \cdot k_2^+ \cdot K_1 \cdot f_{CH_3OH}{}^2 \cdot \theta_d \left(1 - \frac{1}{K_1 \cdot K_2} \cdot \frac{f_{DME} \cdot f_{H_2O}}{f_{CH_3OH}{}^2}\right) \quad \text{(eq S29)}$$

The global equilibrium constant is the multiplication of the elementary equilibrium constants:

$$K_{P,\ Dehyd}^{0} = K_1 \cdot K_2 \quad \text{(eq S30)}$$

The kinetic constant of the global reaction groups the following parameters:

$$k_{Dehyd} = k_2^+ \cdot K_1 = exp\left(k_{0,Dehyd} - \frac{E_{A,Dehyd}}{R \cdot T}\right) \quad \text{(eq S31)}$$

The final reaction rate equation of the methanol dehydration to DME (eq S32) is derived by substituting eqs. S30-S31 into eq S29:

$$r_2 = m_{FER} \cdot exp\left(k_{0,Dehyd} - \frac{E_{A,Dehyd}}{R \cdot T}\right) \cdot \theta_d \cdot f_{CH_3OH}{}^2 \cdot \left(1 - \frac{f_{DME} \cdot f_{H_2O}}{K_{P,\ Dehyd}^{0} \cdot f_{CH_3OH}{}^2}\right) \quad \text{(eq S32)}$$

# Literature


1. B. Lacerda de Oliveira Campos, K. Herrera Delgado, S. Wild, F. Studt, S. Pitter and J. Sauer, *Reaction Chemistry & Engineering*, 2021, **6**, 868-887.
2. D. Surek and S. Stempin, *Angewandte Strömungsmechanik für Praxis und Studium*, B.G. Teubner Verlag / GWV Fachverlage GmbH, Wiesbaden, 2007.
3. W. Bohl and W. Elmendorf, *Technische Strömungslehre: Stoffeigenschaften von Flüssigkeiten und Gasen*, Vogel Buchverlag, Würzburg, 2008.
4. S. Polierer, D. Guse, S. Wild, K. Herrera Delgado, T. N. Otto, T. A. Zevaco, M. Kind, J. Sauer, F. Studt and S. Pitter, *Catalysts*, 2020, **10**, 816-833.
5. H. E. Swanson, M. I. Cook, E. H. Evans and J. H. deGroot, *Standard X-ray Diffraction Powder Patterns*, The National Bureau of Standards, Washington D.C., 1960.
6. A. C. Roberts, J. L. Jambor and J. D. Grice, *Powder Diffraction*, 1986, **1**, 56-57.
7. N. Doebelin and R. Kleeberg, *Journal of applied crystallography*, 2015, **48**, 1573-1580.
8. M. Behrens, F. Girgsdies, A. Trunschke and R. Schlögl, *European Journal of Inorganic Chemistry*, 2009, **2009**, 1347-1357.
9. N. Brese, M. O'keeffe, B. Ramakrishna and R. Von Dreele, *Journal of Solid State Chemistry*, 1990, **89**, 184-190.
10. H. Sawada, R. Wang and A. W. Sleight, *Journal of Solid State Chemistry*, 1996, **122**, 148-150.
11. A. A. Arvidsson, P. N. Plessow, F. Studt and A. Hellman, *The Journal of Physical Chemistry C*, 2020, **124**, 14658-14663.